

Mechanical Design and Rotor-dynamic Analysis of the ORCHID Turbine

Matteo Majer¹, Steven Chatterton², Ludovico Dassi², Alessio Secchiaroli¹, Edoardo Gheller², Carlo De Servi¹, Paolo Pennacchi², Piero Colonna¹, Matteo Pini^{1,*}

¹ *Propulsion and Power, Delft University of Technology, Delft, The Netherlands*

² *Department of Mechanical Engineering, Politecnico di Milano, Milano, Italy*

*Corresponding Author: m.pini@tudelft.nl

ABSTRACT

The ORCHID turbine is a 10 kW, high-speed (~100 krpm) radial-inflow organic Rankine cycle (ORC) turbine, under realization in the Propulsion and Power laboratory of Delft University of Technology. The turbine will be installed and tested in the Organic Rankine Cycle Hybrid Integrated Device (ORCHID) facility, the setup for fundamental and applied studies on ORC technology currently in operation in the same lab. Experimental data from future measurement campaigns will be employed to validate numerical tools and develop best practices for designing and operating these unconventional machines.

This work documents the recent design efforts to define the functional requirements, the necessary components, and the mechanical assessment of the turbine test bed. In particular, the detailed design of the rotor assembly, carried out in cooperation with the Rotor-dynamic research group of Politecnico di Milano, is described with emphasis on three main aspects. First, the derivation of the damping characteristics of a squeeze-film-damper cartridge for turbochargers, which has been selected as support bearing for the turbine shaft. Secondly, the estimation of the stiffness and damping coefficients of a labyrinth gas seal with swirl breakers, using 3D CFD simulations of the flow path. Finally, linear elastic rotordynamic simulations were performed on a finite beam element model of the resulting turbine shaft. The bearing stiffness, initially estimated using Hertz contact theory, was varied to investigate the sensitivity of the rotor critical speeds to it.

535

1 INTRODUCTION

The high-speed, supersonic radial-inflow turbine (sRIT) is the core component of high-temperature organic Rankine cycle (ORC) turbogenerators of power capacity in the 5-100 kW range. These energy conversion systems can be utilized for recovering discharged thermal energy from airborne systems (Perullo, et al., 2013), propulsive engines (Glensvig, et al., 2016), gas turbines for stationary power generation (Cerza, et al., 2022), and flow streams of industrial processes (Wieland, et al., 2023). Several past works (De Servi, et al., 2019), (Cappiello & Tuccillo, 2021), (Cappiello, et al., 2022) document best practices for the optimal design of sRIT and show that comparatively high fluid-dynamic efficiency (~80-85%) can be attained. An experimental verification of their performance is however lacking and, accordingly, a validation of the methods and tools used for their design has not been performed yet.

The ORCHID turbine is a 10 kW, high-speed (~100 krpm) radial-inflow organic Rankine cycle (ORC) turbine, operating with siloxane MM. This machine will be installed and employed for experimental research in the organic Rankine cycle hybrid integrated device (ORCHID) (Head, 2021), in operation at the aerospace propulsion and power laboratory (APP-lab) of Delft University of Technology. Data derived from future measurement campaigns will serve to i) demonstrate that the high fluid-dynamic performance of RIT predicted by theoretical and numerical studies (De Servi, et al., 2019) are achievable in practice ii) validate the numerical tools employed for the design of these highly unconventional turbines, and iii) develop experience and best practices for their optimal operation, including the thermal management of the bearings system.

Experimentally characterizing the fluid-dynamic performance of small-scale ORC turbines requires a setup that can, most importantly, enable stable and safe operation of the machine from start-up up to nominal design point, and at off-design conditions. A few test benches for small-scale ORC turbines

are currently operational throughout Europe. In 2017, the TFD institute at Leibniz University in Hannover (Seume, et al., 2017) has developed a facility for testing a small-scale, 10kW axial flow impulse turbine operating with ethanol and featuring partial admission nozzles. The rotational velocity at the design point is 100 krpm, while the maximum stage pressure ratio of ~ 50 was achieved in the half admission operation. The rotor is supported on custom, high precision ball bearings and forms a single turbine-generator unit. More recently, LUT University (Uusitalo, et al., 2020) has commissioned a test facility resembling an organic Rankine cycle turbogenerator and featuring a ~ 12 kW radial inflow turbine operating with siloxane MDM as expander. The turbine stage was designed to operate at 31500 rpm, with a total-to-static pressure ratio of ~ 112 . The rotor is supported on hydrodynamic bearings operating with MDM in liquid phase and is equipped with a permanent magnet generator for shaft to grid power conversion. Finally, the Laboratory of Applied Mechanical Design of EPFL (Rosset, et al., 2021) successfully designed, constructed, and operated a R245fa radial-inflow turbine at the nominal speed of 100 krpm, measuring a power output of 2.3 kW. The rotor is supported on custom designed gas-lubricated bearings, allowing smaller drag torque compared to liquid lubricated bearings, and offering an efficient oil-free solution for the low power range. Other facilities include (Kang, 2016), (Weiß, et al., 2018), (Klonowicz, et al., 2014), showcasing the increasing interest for small-scale ORC applications throughout Europe and beyond.

Given the notable advantages offered by gas lubricated bearings compared to systems relying on oil lubrication, most importantly the avoidance of working fluid contamination and complexity/weight reduction of the turbine assembly, their adoption to support rotors of sRIT is arguably the best option. However, for machines in which the flow conditions lead to an axial thrust of the order of 100 N, like in the case of the ORCHID turbine, their design still represents a challenge. To reduce the risks associated to the development of a high-speed rotor based on gas dynamic bearings, the first prototype of the ORCHID turbine rotor integrates more conventional rolling element bearings, a choice which also enables the use of off-the-shelf components.

In this paper, the layout of ORCHID turbine rotor and the mathematical modeling of the various parts of the assembly for the rotordynamic analysis are described. A pocket damper gas seal was designed for secondary flows management and, to support the powertrain over the operating envelope, an off-the-shelf rolling element bearings (REB) cartridge with a squeeze-film-damper (SFD) was characterized. Finally, the sensitivity of the dynamic stability characteristics of the turbine rotor to some of the design parameters was investigated, using the results of a rotordynamic calculation performed with a computer program developed in-house by Politecnico di Milano.

2 MECHANICAL DESIGN

2.1 Preliminary design

Fundamental requirements for a rotating test rig for academic research include the possibility to test at different speeds and thermodynamic conditions, and tear-down / mounting easiness of the assembly to speed-up the test campaign preparation and execution. Such characteristics result from careful and informed choices on the mechanical design and components employed in the facility.

Three main technical aspects were considered a-priori in the conceptual design phase:

1. The turbine arrangement (straddled or overhung rotor)
2. The type of bearings (gas-dynamic, rolling element or active magnetic bearings)
3. The sealing strategy, intimately linked to the bearings type and turbine arrangement

Figure 1a shows the straddled rotor configuration, in which the turbine wheel is placed within two bearings. Figure 1 b instead shows an example of overhung impeller configuration, with the wheel mounted outboard on the right-hand side. Straddled rotors are arguably more robust and lead to smaller shaft deflections, but the presence of bearings on each side of the wheel calls for a more complex assembly. Conversely, overhung impellers result in a less complex and easier to access assembly, though the rotordynamic design is typically more challenging.

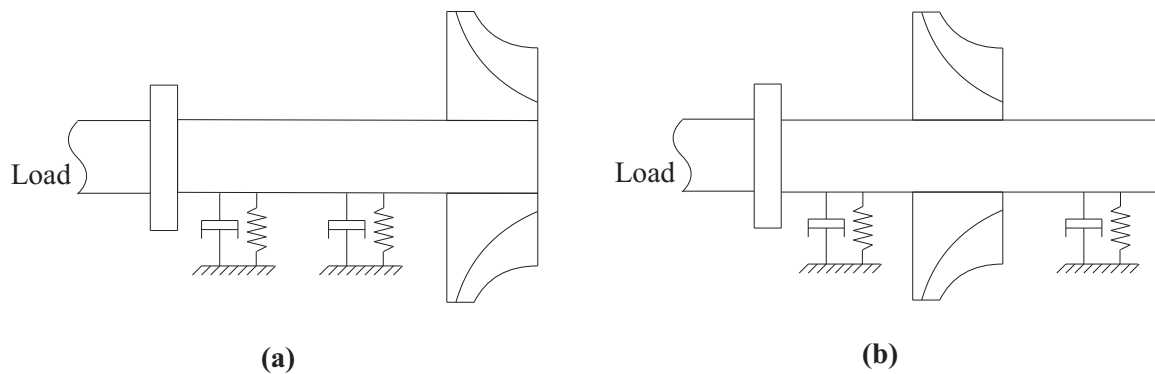


Figure 1 Rotor configuration concepts. a) Straddled impeller, and b) overhung impeller configuration.

The use of ceramic ball bearings for a concept turbine of this type has two main advantages over competing technologies. Firstly, they can handle substantially higher loads than gas lubricated bearings, offering a robust solution in a wide range of working conditions. Secondly, thanks to the widespread use of REB in a plethora of applications, they are available off-the-shelf and can be readily implemented within a new design. Recent trends in turbocharger systems show that rolling element bearings can be used in compact, mobile systems such as automotive turbo-chargers (Schweitzer & Adleff, 2006), offering long term durability with comparable lubrication and mechanical losses with respect to non-contact bearings at high speeds (Nguyen-Schäfer, 2012).

Albeit the use of REB simplifies the assembly design, the presence of lubricant in the system poses additional challenges compared to gas bearings. The cross contamination of the main working fluid and the lubricant can severely impact the performance and integrity of the entire rig. Lubricant contamination of the working fluid loop could lead to poor turbine efficiency and mechanical damage of the rotating components due to erosion. Moreover, leaked oil could accumulate and form hot spots in the closed-loop, increasing the risk of thermal decomposition of siloxane MM. On the other hand, the leakage of MM vapour within the machine casing can cause overheating and poor reliability of the bearings. Therefore, the choice of a proper sealing technology is key to ensure safe and reliable operation.

To seal the machine from oil leaks towards the working fluid loop, a common strategy adopted for large steam power plants is to use a dry-gas seal system (Forsthoffer, 2011), employing an inert gas as a barrier between the two flows to be sealed. As an alternative, contact seals are commonly employed in automotive and guarantee perfect oil sealing. The advantage of the dry-gas solution is the absence of contact parts between the stationary and the rotating components, but this comes at the cost of a more complex rotor design. In fact, the presence of the dry-gas requires more components (for sealing the different flows) and more complex control strategies. Conversely, the contact seal solution leads to a simpler and more compact assembly. Thanks to comparatively lower rotational speed and maximum operating temperatures of ORC turbines, with respect to similar size gas turbines, off-the-shelf lip seals can theoretically be used. Advancements in low friction materials development and temperature resistant coatings enable state-of-art contact seals to operate at peripheral speeds up to 100 m/s in combination with temperatures in excess of 200°. Therefore, PTFE based lip seals were deemed appropriate for this application upon verification with a manufacturer.

The conceptual layout obtained in the initial design phase resulted, after several design iterations, in the rotor configuration shown in Figure 2. The rotor includes a shaft (A), a turbocharger cartridge (B), a turbine wheel (C), and a coupling flange (D). A lock-nut on the left side of the bearing inner raceway (E) is used to regulate the mounted-end-play (MEP) of the rolling elements by adjusting the preload. The cartridge pries axially against a stainless steel thin-disk (F), with the function of moving the oil outwards to the oil drain lines machined in the casing (not visible in figure).

Stationary parts include two off-the-shelf lip seals (G and H) to contain the oil within the turbine casing, and an in-house developed gas seal (J) to limit the leakage of siloxane vapour from the turbine flow-path.

2.2 Characterization of the dynamic response of an SFD

The bearing cartridge has the main function of supporting the powertrain and transfer all loads to the structure. A three-dimensional representation of the bearing cartridge is shown in Figure 3. The cartridge inner ring is fitted to the turbine shaft, while the outer ring has a clearance fit with the casing. Two rows of rolling elements are interposed between the two rings. The outer ring is axially locked in the casing using a snap-ring (K in Figure 2), while a rectangular slot and pin system (L in Figure 2) is used to lock it circumferentially.

The two regions highlighted in red in Figure 3 act as squeeze-film-dampers (SFD's). The clearance fit of 50 μm between the outer ring and the casing ensures that, as a result of lateral motion of the powertrain, the outer ring squeezes the oil film in the gap, resulting in film pressurization.

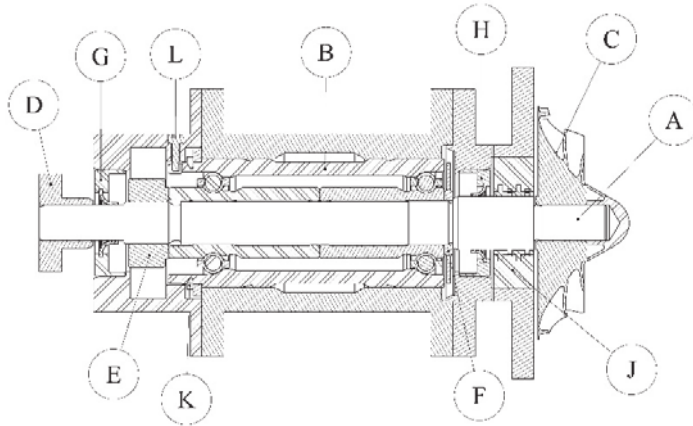


Figure 2 ORCHID turbine cross-section

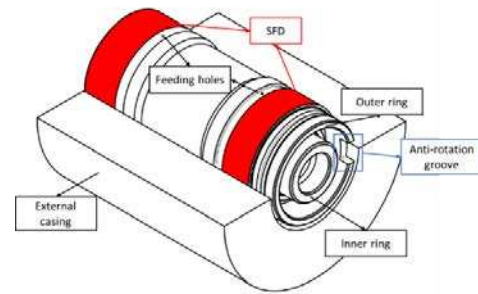


Figure 3 Detail of the REB cartridge

Such pressure introduces damping in the system and can be modelled according to the Reynolds equation (1).

$$\frac{\partial}{R\partial\theta}\left(\frac{\rho h^3}{12\mu}\frac{\partial P}{R\partial\theta}\right) + \frac{\partial}{\partial z}\left(\frac{\rho h^3}{12\mu}\frac{\partial P}{\partial z}\right) = \frac{\partial}{\partial t}(\rho h) + \frac{\rho h^2}{12\mu}\frac{\partial^2 \rho h}{\partial t^2} \quad (1)$$

Where ρ and μ are the oil density and dynamic viscosity, θ and z are the tangential and axial coordinates, while h is the oil film thickness, and P is the oil pressure.

The last term on the right-hand side of Equation (1) represents the temporal inertia contribution. This term has a significant effect on the pressure distribution if the oil film Reynolds number $Re_s = \frac{\rho\omega g^2}{\mu} > 1$, where ω is the whirling frequency and g is the clearance of the SFD gap (Delgado & San Andres, 2010). In the present case, assuming ISO VG 32 as lubricant we obtain $Re_s < 1$ throughout the operating range of the machine. Therefore, the temporal inertia term contribution is neglected in the SFD analysis.

The motion of the outer ring is modeled as a circular centered orbit. Equation (2) describes the oil film thickness distribution.

$$h(\theta, t) = g - (e \cos \omega t) \cos \theta - (e \sin \omega t) \sin \theta \quad (2)$$

where e is the radius of the orbit described by the SFD in the plane orthogonal to its axis, and ω its whirling frequency. The orbit can either be a circular or elliptical path resulting from lateral vibrations of the cartridge, originating from the rotor unbalance. Thus, the whirling frequency corresponds – for this particular case – to the shaft rotational frequency.

Due to the high operating speed of the turbine, and the small radial gap of the SFD, oil cavitation may occur (Zeidan & Vance, 1990). Thus, equations (1) and (2) are complemented with a model to predict cavitation as proposed by (Almqvist, et al., 2014), imposing ambient pressure at the two sides of each SFD as a boundary condition.

The pressure distribution is calculated for several shaft positions within a circular orbit and the orbit-based dynamic damping coefficient C is calculated as in (San Andres & Jeung, 2016). The evolution of the dynamic damping coefficients with respect to the speed and the orbit radius $e_r = e/g$ relative to the SFD gap is shown in Figure 4.

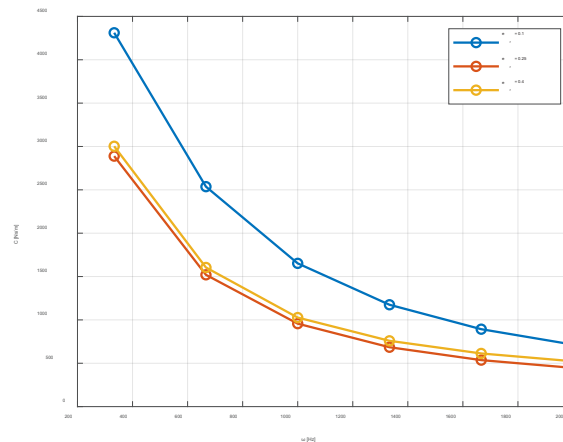


Figure 4 SFD damping coefficient as function of the orbit frequency and the eccentricity.

The damping coefficient of the SFD decreases as a function of the orbit frequency. This trend is to be expected, due to the increasingly higher amount of evaporated oil within the film at higher rotational speed. Previous study on oil cavitation in SFD (Zeidan & Vance, 1990) showed that once the so called “bubbly region” is reached, oil pressure and thus damping characteristics stabilize even with further increase of the rotational speed. Moreover, larger SFD vibrations (thus larger orbits) cause larger pressure differences within the oil film (San Andres & Jeung, 2016), causing larger portions of the film to cavitate. Nevertheless, once the maximum cavitation limit is reached (Zeidan & Vance, 1990), oil pressure and damping characteristics are less sensitive to further increases in eccentricity. This is the reason why the curves for $e_r = 0.25$ and 0.4 in Figure 4 are almost superimposed despite the increasing orbit radius.

To conclude, a progressive degradation of system stability at high speed is expected as a result of enhanced oil cavitation rate in the SFD.

2.3 Design and characterization of a pocket-damper gas seal

A pocket damper gas seal was developed to prevent excessive leak of siloxane MM from the ORCHID closed-loop and provide additional damping to the rotor system. Figure 5 a shows the geometry of the seal. The part was designed as a single body, hollow disk made of stainless steel with four rows of pockets acting as labyrinths. Adjacent rows of pockets were shifted relatively to each other to avoid preferential paths for the leaking gas. The pockets extend 50° circumferentially and 1 mm axially to guarantee feasibility with additive manufacturing methods.

RANS simulations of the flow within the gas seal were carried out using ANSYS Fluent on the computational domain of Figure 5 b. The domain was extended at the inlet and outlet of the clearance gap between the seal inner surface and the shaft surface to avoid boundary conditions influencing the flow solution. Table 1 reports the boundary conditions of pressure and temperature imposed. The domain was discretized with 5.1 M cells based on the results of a mesh independence study. The hybrid mesh included a structured layer of 10 cells to resolve the boundary layer on the no-slip walls of shaft and gas seal inner surface. The SST $k-\omega$ model was used for turbulence closure, while look-up tables generated using REFPROP were employed to model the fluid properties.

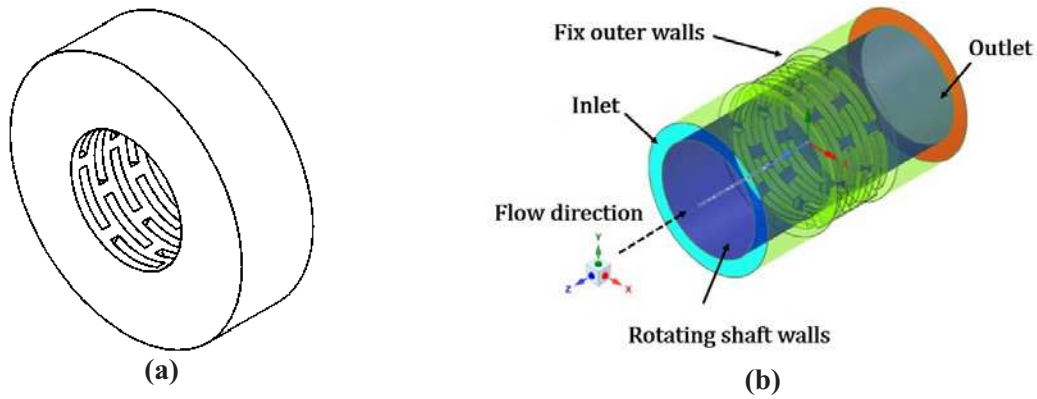


Figure 5 Pocket damper seal. On the left, seal design and main dimensions. On the right, computational domain for CFD simulations and boundary conditions.

Table 1 Boundary conditions for gas seal CFD simulations

Quantity	Inlet	Outlet
Pt	1.73 bar	
Tt	534 K	
P		1.013 bar

Lateral shaft displacement and displacement rates (Δx and $\Delta \dot{x}$) of the rotating shaft wall were imposed. The magnitude of these was determined by means of a convergence study, where their value was varied until the stiffness and damping coefficients stabilized.

Simulations at shaft rotational speed going from 20 to 100 krpm were carried out to investigate the impact of the gas seal on system stability at different speeds.

A nominal radial gap between the inner seal and the shaft outer surface of 50 μm was chosen, that is the same allowed by the SFD. The leakage mass-flow rate of siloxane MM computed from CFD was ~ 1 g/s, and it was verified to vary linearly as a function of the radial clearance.

The resulting forces in the horizontal and vertical directions F_x and F_y were calculated by integration of the pressure field on the shaft outer surface. The direct and cross-term stiffness and damping coefficients were calculated according to their definitions, as follows:

$$k_{xx} = \frac{F_x - F_{x_0}}{\Delta x}; k_{yx} = \frac{F_y - F_{y_0}}{\Delta x}; c_{xx} = \frac{F_x - F_{x_0}}{\Delta \dot{x}}; c_{yx} = \frac{F_y - F_{y_0}}{\Delta \dot{x}}$$

where the denominators are the imposed displacement and displacement rate previously introduced. F_{x_0} and F_{y_0} are the aerodynamic forces with null shaft displacement.

Figure 6 shows the computed stiffness and damping coefficients at varying rotational speed of the rotor shaft. Direct terms show a weak dependence on the rotational speed, while cross-terms increase linearly. From a rotordynamic standpoint, the system stability will be negatively affected by the presence of the gas seal as the speed is increased, due to the increasing cross-terms of the stiffness matrix. Cross-coupled stiffness has an important effect only when its magnitude is comparable to the direct terms. In this case, the cross-coupled terms of the gas seal stiffness matrix are relevant at the design speed, as shown by the left-hand graph of Figure 6, and will therefore be accounted for in the rotordynamic analysis.

Cross-coupled damping terms are instead significantly lower than the direct ones, suggesting that their influence on system stability will be rather low. Nevertheless, since their value has a comparable order of magnitude than that of the direct terms, they must be included in the rotordynamic analysis.

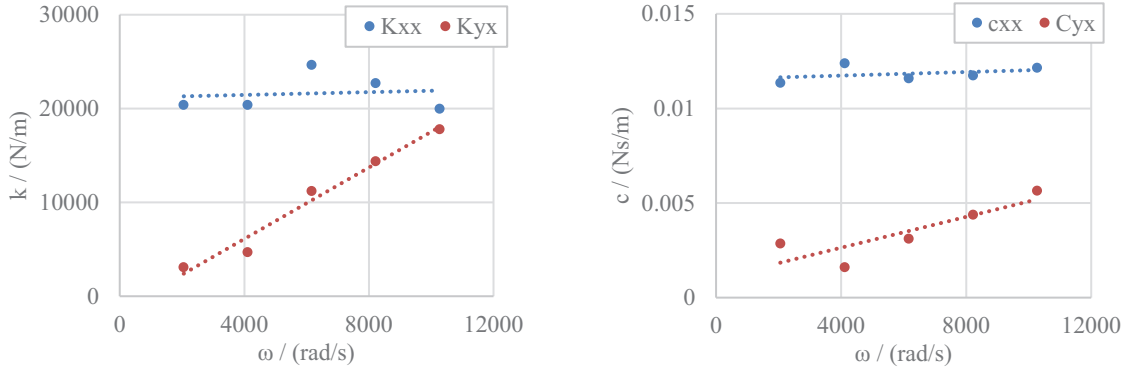


Figure 6 Stiffness (left) and damping (right) coefficients from CFD simulations. Dotted lines represent the linear fit used as input for the rotordynamic analysis.

3 ROTORDYNAMIC ANALYSIS

The dynamic behavior of the machine has been investigated by means of a rotordynamic model of the machine-train. The model includes the finite beam element model of the shaft train, that of the REB cartridge and its SFD characteristics, the gas seal and the cross-coupled aerodynamic forcing of the turbine wheel (San Andres, 2023). The resulting finite element representation of the machine is shown in Figure 7, together with the non-rotating cartridge outer ring. The rotating parts include the coupling hub flange, the bearing lock-nut, the cartridge inner ring, the impeller and the ogive. The effect of the coupling shaft mass and inertia is introduced as a lumped mass on the second node from the left in Figure 7.

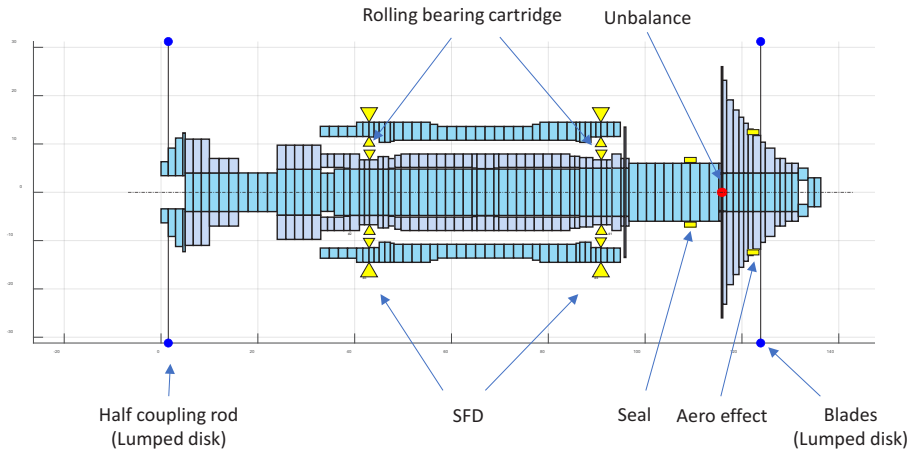


Figure 7 Rotordynamic model showing the mass distribution of the rotor discretized using disks.

The equation of motion of the structure is described by Equation (3):

$$[M]\ddot{\mathbf{x}} + ([C] + \Omega[G])\dot{\mathbf{x}} + [K]\mathbf{x} = \mathbf{F} \quad (3)$$

Where $[M]$, $[C]$, $[G]$ and $[K]$ are respectively the mass, damping, gyroscopic, and the stiffness matrix, while \mathbf{F} is the array of unbalance forces.

The dynamic behaviour of the REB is represented by linearized coefficients using the classical stiffness and damping matrices.

$$[K]^{REB} = \begin{bmatrix} k_{xx}^{REB} & 0 \\ 0 & k_{xx}^{REB} \end{bmatrix}; [C]^{REB} = \begin{bmatrix} c_{xx}^{REB} & 0 \\ 0 & c_{xx}^{REB} \end{bmatrix}; [K]^{aero} = \begin{bmatrix} 0 & k_{xy}^{aero} \\ -k_{xy}^{aero} & 0 \end{bmatrix}$$

$[K]^{REB}$ and $[C]^{REB}$ are diagonal matrices because the stiffness and damping cross-terms are negligible for such bearings. The stiffness coefficients used in this study were provided by the bearing manufacturer, computed by means of Hertz contact theory, expressed as a function of the load acting on the bearing. The load depends on the radial and thrust aerodynamic forces, changing with the

rotational speed. $[K]^{aero}$ is the matrix of the aerodynamic forces brought in by the impeller, with non-zero cross-terms and negligible direct terms. The destabilizing cross-term $k_{xy}^{aero} = 633.75e3$ N/m was determined using Wachel's formula, according to a level I analysis as per the API 617 norm for radial expander-compressor systems (API 617, 2014).

The effect of the squeeze-film-damper is considered through a damping matrix with equal direct terms, in which the direct damping coefficient is evaluated by means of the Reynolds model described earlier. Instead, the effect of the seal is included using a stiffness and a damping matrix, both with equal direct terms and opposite cross-terms, estimated by means of CFD simulations for several rotational speeds.

$$[C]^{SFD} = \begin{bmatrix} c_{xx}^{SFD} & 0 \\ 0 & c_{xx}^{SFD} \end{bmatrix}; [K]^{seal} = \begin{bmatrix} k_{xx}^{seal} & k_{xy}^{seal} \\ -k_{xy}^{seal} & k_{xx}^{seal} \end{bmatrix}; [C_{seal}] = \begin{bmatrix} c_{xx}^{seal} & c_{xy}^{seal} \\ -c_{xy}^{seal} & c_{xx}^{seal} \end{bmatrix},$$

The result of the eigenfrequency analysis as a function of the rotational speed is reported in the Campbell diagram of Figure 8. The critical speeds for excitations up to the 2X component, along with the corresponding damping factors in the range from 20krpm to 120krpm are listed in Table 2.

The first 4 mode shapes are mainly rigid modes of the shaft and cartridge relative movement, whereas modes 5 to 8 include the bending of the shaft.

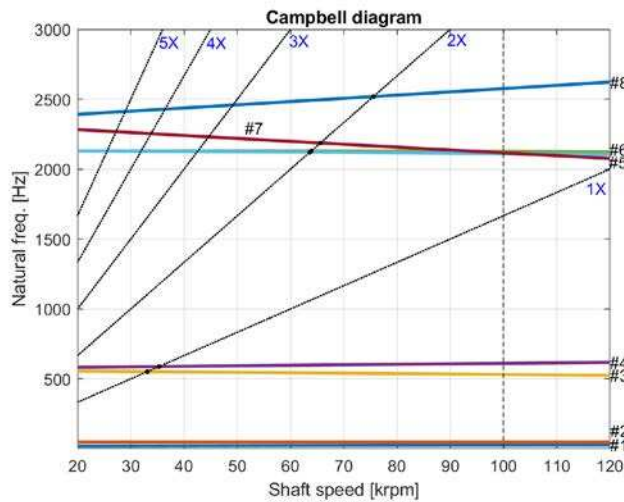


Table 2 Critical speed and damping ratio of mode 3 to mode 8 when crossing the 1X and 2X shaft frequency excitation

Mode #	Critical speed [krpm]	Damping ratio
3	33.1	0.093
4	35.3	0.377
5	63.8	0.584
6	63.6	0.599
7	65.6	0.134
8	75.5	0.181

Figure 8 Campbell diagram of the ORCHID turbine rotor

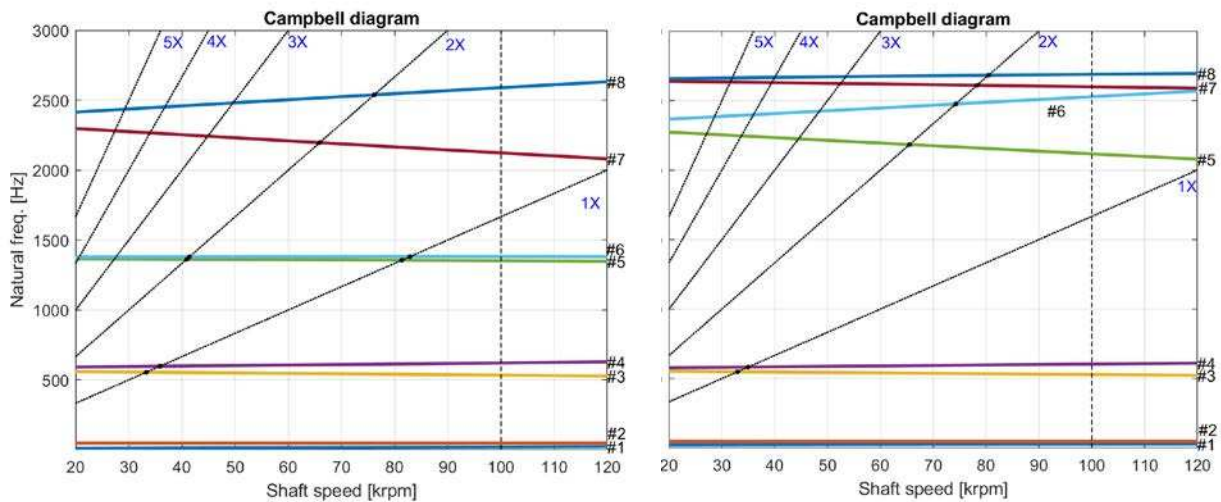


Figure 9 Campbell diagrams of rotor dynamic response using -30% (left) and +30% (right) of the bearing stiffness calculated through Hertzian contact theory

The Campbell diagrams for the change of the stiffness coefficient of the rolling element bearing cartridge, varied in the range $\pm 30\%$ with respect to the nominal values, is shown in Figure 9.

The eigenfrequencies of the first 4 rigid modes remain unchanged, whereas those of modes 5 to 8 increase with the increase of the bearing stiffness. Modes 5 and 6 are critical because critical speeds can arise within the operating range of the machine, which is the region going from 80 to 120 krpm. The response to the unbalance at the design rotational speed of 100 krpm has an amplitude $< 1 \mu\text{m}$, almost 2 orders of magnitude lower than the gas seal and SFD radial clearances.

The stability of the shaft train has been verified by progressively increasing the stiffness cross-terms of the aerodynamic forcing matrix $[K]^{aero}$. Mode #3 becomes unstable ($h < 0$) even with low values of k_{xy}^{aero} but, since it is a rigid backward mode between the shaft and the REB cartridge, it is not critical.

4 CONCLUSIONS

The current work documents the preliminary design and rotordynamic analysis of the high-speed rotor of the ORCHID turbine. The damping coefficient of a cartridge for turbochargers, featuring a $50 \mu\text{m}$ squeeze-film-damper, has been characterized throughout the entire rotational speed envelope. The stiffness and damping coefficients of a pocket damper gas seal designed in-house were calculated using CFD simulations, showing that the cross-coupled stiffness coefficients have a non-negligible effect on the rotordynamics. The frequency analysis of the first 8 mode shapes highlighted the presence of 4 rigid modes (1 to 4) and 4 flexible modes (5 to 8). Rotordynamic analyses of the assembly, including the stiffness of the bearings coefficients according to Hertz theory, shows a large sensitivity of the first two flexible shaft modes (mode 5 and 6) to bearing stiffness variations in the range $\pm 30\%$. In particular, mode 5th leads to a potentially critical frequency in the operating range of the machine, depending on the actual bearing stiffness coefficient. At present time, a conclusive analysis of the dynamic performance of the machine designed in this work is still lacking. Given that the modeling assumptions have significant impact on the results of the present investigation, a comprehensive sensitivity study is envisaged as future work to eventually determine the optimal powertrain design. Finally, future real life balancing and testing will provide the necessary level of confidence on the results here described.

543

NOMENCLATURE

C	Damping coefficient	(Ns/m)	T	Temperature	(K)
E	eccentricity	(μm)	Tt	Total Temperature	(K)
F	Force	(N)	x	Displacement	(m)
g	SFD gap	(μm)	\dot{x}	Velocity	(m/s)
K	Stiffness coefficient	(N/m)	\ddot{x}	Acceleration	(m/s ²)
\dot{m}	Mass-flow rate	(g/s)	θ	Angular coordinate	(rad)
M	Mass	(kg)	μ	Dynamic viscosity	(Pa s)
P	Pressure	(Pa)	ρ	Density	(kg/m ³)
Pt	Total Pressure	(Pa)	ω	Angular velocity	(rad/s)
t	Time	(s)	Ω	Rotational velocity	(rpm)

REFERENCES

- Almqvist, A., Fabricius, J., Larsson, R. & Wall, P., 2014. A New Approach for Studying Cavitation in Lubrication. *Journal of Tribology*, Volume 136.
- API 617, 2014. *Axial and Centrifugal Compressors and Expander-Compressors for Petroleum, Chemical and Gas Industry*. s.l.:s.n.
- Cappiello, A., Majer, M., Tuccillo, R. & Pini, M., 2022. *On the Influence of Stator-Rotor Radial Gap Size on the Fluid-Dynamic Performance of Mini-ORC Supersonic Turbines*. s.l., ASME, p. 15.
- Cappiello, A. & Tuccillo, R., 2021. Design Parameter Influence on Losses and Downstream Flow Field Uniformity in Supersonic ORC Radial-Inflow Turbine Stators. *Int. J. Turbomach. Propuls. Power*.

- Cerza, M., Meinster, B. & Blair, C. S., 2022. *Implementation of a Waste Heat Recovery Combined Cycle System Employing the Organic Rankine Cycle for a Gas Turbine*. s.l., AIAA.
- De Servi, C. M. et al., 2017. *Exploratory Assessment of a Combined Cycle Engine Concept for Aircraft Propulsion*. Zurich, s.n.
- De Servi, C. M., Burigana, M., Pini, M. & Colonna, P., 2019. Design Method and Performance Prediction for Radial-Inflow Turbines of High-Temperature Mini-Organic Rankine Cycle Power Systems. *J. Eng. Gas Turbines Power*, 141(9), p. 12.
- Delgado, A. & San Andres, L. A., 2010. Model for Improved Prediction of Force Coefficients in Grooved Squeeze-film-dampers and Oil Seal Rings. *Journal of Tribology*, Volume 132, pp. 1-12.
- Forsthoffer, W. E., 2011. Dry Gas Seal Best Practices. In: *Forsthoffer's Best Practice Handbook for Rotating Machinery*. s.l.:Elsevier, pp. 501-524.
- Glensvig, M., Schreier, H., Tizianel, M. & Theissl, H., 2016. Testing of a Long-Haul Demonstrator Vehicle with a Waste Heat Recovery System on Public Road. *SAE Technical Paper*, pp. 1-9.
- Head, A. J., 2021. *Novel Experiments for the Investigation of Non-Ideal Compressible Fluid Dynamics*. Delft(South-Holland): TU Delft.
- Kang, S. H., 2016. Design and preliminary tests of ORC (organic Rankine cycle) with two-stage radial turbine. *Energy*, Volume 96, pp. 142-154.
- Klonowicz, P. et al., 2014. Design and performance measurements of an organic vapour turbine. *Applied Thermal Engineering*, 63(1), pp. 297-303.
- Nguyen-Schäfer, H., 2012. *Rotordynamics of Automotive Turbochargers*. Berlin: Springer Berlin, Heidelberg.
- Perullo, C., Mavris, D. & Fonseca, E., 2013. *An Integrated Assessment of an Organic Rankine Cycle Concept for Use in Onboard Aircraft Power Generation*. San Antonio, ASME.
- Rosset, K., Pajot, O. & Schiffmann, J., 2021. Experimental Investigation of a Small-Scale Organic Rankine Cycle Turbo-Generator Supported on Gas-Lubricated Bearings. *J. Eng. Gas Turbines Power*, 143(5), p. 14.
- San Andres, L., 2023. A Review of Turbine and Compressor Aerodynamic Forces in Turbomachinery. *Lubricants*, p. 22.
- San Andres, L. & Jeung, S. H., 2016. Orbit-Model Force Coefficients for Fluid Film Bearings: A Step beyond Linearization. *Journal of Engineering for Gas Turbines and Power*, Volume 138.
- Schweitzer, F. & Adleff, K., 2006. Rolling bearings in turbocharger applications. *MTZ worldwide*, Volume 67, pp. 16-19.
- Seume, J. R., Peters, M. & Kunte, H., 2017. *Design and test of a 10kW ORC supersonic turbine generator*. s.l., IOP Publishing Ltd, p. 10.
- Uusitalo, A., Turunen-Saaresti, T., Honkatukia, J. & Dhanasegaran, R., 2020. Experimental study of small scale and high expansion ratio ORC for recovering high temperature waste heat. *Energy*, Volume 208.
- Weiß, A. et al., 2018. Experimental characterization and comparison of an axial and a cantilever micro-turbine for small-scale Organic Rankine Cycle. *Applied Thermal Engineering*, Volume 140, pp. 235-244.
- Wieland, C., Schifflechner, C., Dawo, F. & Astolfi, M., 2023. The organic Rankine cycle power systems market: Recent development and future perspectives. *Applied Thermal Engineering*, Volume 224.
- Zeidan, F. Y. & Vance, J. M., 1990. Cavitation Regimes in Squeeze-film-dampers and Their Effect on the Pressure Distribution. *Tribology Transactions*, 33(3), pp. 447-453.

ACKNOWLEDGEMENT

The authors would like to acknowledge NWO and the industrial partners of the ARENA project, whose funding grant made this research possible. Moreover, the data and expertise the cartridge manufacturer (and all industrial partners) contributed with was fundamental for the design and modeling presented.